

Article

# Self-Assembly of Porous Hierarchical BiOBr Sub-Microspheres for Efficient Aerobic Photooxidation of Benzyl Alcohol under Simulated Sunlight Irradiation

Zhigang Wang<sup>1</sup>, Cheng Liu<sup>2,3</sup>, Fengxi Chen<sup>2</sup>  and Rong Chen<sup>2,4,\*</sup> <sup>1</sup> School of Chemistry and Chemical Engineering, Hubei Polytechnic University, Huangshi 435003, China<sup>2</sup> State Key Laboratory of New Textile Materials & Advanced Processing Technologies, Wuhan Textile University, Wuhan 430200, China<sup>3</sup> School of Chemistry and Environmental Engineering, Wuhan Institute of Technology, Wuhan 430205, China<sup>4</sup> Henan Institute of Advanced Technology, Zhengzhou University, Zhengzhou 450002, China

\* Correspondence: rchenhku@hotmail.com

**Abstract:** Semiconductor photocatalytic performances can be modulated through morphology modification. Herein porous hierarchical BiOBr microspheres (BiOBr-MS) of ~3 μm was firstly self-assembled without the assistance of a template via a facile solvothermal synthesis in triethylene glycol (TEG) at 150 °C for 3 h. KBrO<sub>3</sub> was exploited as a bromine source, which slowly provided bromide ions upon reduction in TEG and controlled the growth and self-assembly of primary BiOBr nanoplates. The addition of PVP during solvothermal synthesis of BiOBr-MS reduced the particle size by about three-fold to generate BiOBr sub-microspheres (BiOBr-sMS) of <1 μm. BiOBr-sMS exhibited significantly higher photocatalytic activity than BiOBr-MS for aerobic photooxidation of benzyl alcohol (BzOH) to benzaldehyde (BzH) under simulated sunlight irradiation (conversions of BzOH (50 mM) over BiOBr-sMS and BiOBr-MS were, respectively, 51.3% and 29.6% with 100% selectivity to BzH after Xenon illumination for 2 h at 25 °C). The photogenerated holes and ·O<sub>2</sub><sup>-</sup> were found to be main reactive species for the BzOH oxidation over BiOBr spheres by scavenging tests and spin-trapping EPR spectra. The higher photocatalytic activity of BiOBr-sMS was attributed to its more open hierarchical structure, efficient charge separation, more negative conduction-band position and the generation of larger amounts of ·O<sub>2</sub><sup>-</sup>.

**Keywords:** BiOBr spheres; hierarchical nanostructures; photocatalysis; benzaldehyde

**Citation:** Wang, Z.; Liu, C.; Chen, F.; Chen, R. Self-Assembly of Porous Hierarchical BiOBr Sub-Microspheres for Efficient Aerobic Photooxidation of Benzyl Alcohol under Simulated Sunlight Irradiation. *Catalysts* **2023**, *13*, 958. <https://doi.org/10.3390/catal13060958>

Academic Editor: Kangle Lv

Received: 7 May 2023

Revised: 21 May 2023

Accepted: 30 May 2023

Published: 1 June 2023



**Copyright:** © 2023 by the authors. Licensee MDPI, Basel, Switzerland. This article is an open access article distributed under the terms and conditions of the Creative Commons Attribution (CC BY) license (<https://creativecommons.org/licenses/by/4.0/>).

## 1. Introduction

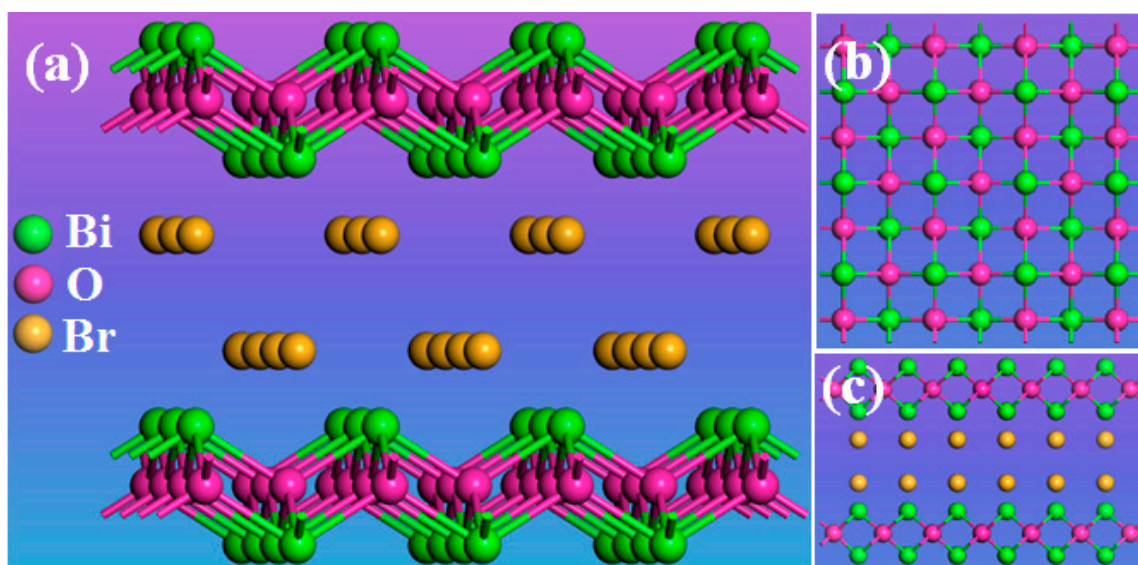
Benzaldehyde (BzH) is an important starting material for the production of some chemical intermediates, dyes, flavors and pharmaceuticals (e.g., benzylamine, benzoin, mandelic acid, triphenylmethane dyes, cinnamaldehyde and chloramphenicol) [1]. It is industrially produced by the hydrolysis of benzal chloride or partial oxidation of toluene [1,2]. The former generates large quantities of HCl as a by-product, while the latter produces BzH only as a by-product in the production of less valuable benzoic acid.

Sunlight-driven photocatalytic aerobic oxidation of benzyl alcohol (BzOH) is a potential green route to synthesize BzH because O<sub>2</sub> is a green oxidant and natural sunlight is clean, safe, widely available and inexhaustible. This technology relies on the design and synthesis of sunlight-responsive semiconductor photocatalysts with suitable conduction and valance-band positions to selectively oxidize BzOH to BzH [3]. In order to utilize solar energy, it is important for potential photocatalysts to harness visible light since UV light only accounts for less than 5% in the whole solar spectrum [4].

Various strategies, including heterojunction construction, doping, noble metal deposition and photosensitization, have been adopted to develop efficient solar photocatalysts for aerobic photooxidation of BzOH. However, most of these methods required complex

architecture engineering with multiple components (e.g.,  $\text{WO}_{2.72}/\text{rGO}$  nanocomposites [5],  $\text{CdS@MoS}_2$  [6], hybrid- $\text{SiW}_{11}\text{O}_{39}$  [7], fluorinated mesoporous  $\text{WO}_3$  [8] and  $\text{Ni-OTiO}_2$  [9]). Therefore, it would be more attractive if a single semiconductor with a narrow-band gap can effectively catalyze the sunlight-driven aerobic photooxidation of BzOH.

Among many visible light-responsive semiconductors (e.g.,  $\text{Pt-BiFeO}_3$  [10],  $\text{Bi}_2\text{WO}_6/\text{ZnO}$  composite [11]), bismuth oxybromide ( $\text{BiOBr}$ ) has attracted considerable attention owing to its unique layered structure, appropriate-band gap ( $\sim 2.7$  eV) and good chemical stability [12,13]. The layered structure of  $\text{BiOBr}$  consists of  $[\text{Bi}_2\text{O}_2]^{2+}$  layers interleaved with double layers of  $\text{Br}^-$  along the  $c$ -axis (Scheme 1), and is beneficial for the separation of photogenerated charge carriers owing to the internal electric field normal to each layer. However, the photocatalytic performance of pure  $\text{BiOBr}$  is still limited due to high recombination rate of photogenerated electron-hole pairs and low quantum efficiency. After visible light ( $>420$  nm) irradiation for 4 h at  $25^\circ\text{C}$ , only 10.9% of BzOH was converted to BzH in the reaction system comprising 20 mg  $\text{BiOBr}$  and 8.0 mM BzOH in 2.5 mL benzotrifluoride (BTF) saturated with  $\text{O}_2$  [14]. Even after visible light ( $>420$  nm) irradiation for 8 h at  $50^\circ\text{C}$ , the conversion of BzOH to BzH was still low (21.6%) in the reaction system comprising 50 mg  $\text{BiOBr}$  and 0.5 mM BzOH in 10 mL  $\text{CH}_3\text{CN}$  in the presence of  $\text{O}_2$  [3].



**Scheme 1.** Structure models of  $\text{BiOBr}$ . (a) Three-dimensional projection, (b)  $[001]$  direction and (c)  $[110]$  direction.

Many efforts have been made to enhance sunlight-driven photocatalytic efficiency of  $\text{BiOBr}$ , including heterojunction construction (e.g.,  $\text{BiOBr}/\text{Bi}_2\text{WO}_6$  [14] and  $\text{CuO-BiOBr}$  [15]), surface regulation (e.g.,  $\text{BiOBr m}$  [16]), metal loading (e.g.,  $\text{Ag-Fe-Cu}/\text{BiOBr}$  [17], Eu-doped  $\text{BiOBr}$  [18]), defect engineering (e.g.,  $\text{BiOBr-OV}$  [19]) and synergistic effects (e.g.,  $\text{Zn-VBOB}$  [20]). It was also reported that morphology control of  $\text{BiOBr}$  (e.g., ultrathin nanosheets and three-dimensional (3D) hierarchical structures) could promote its photocatalytic performances [13,21–24]. Compared with low-dimensional counterparts, three-dimensional hierarchical  $\text{BiOBr}$  microspheres built from nanosheets or nanoplates not only alleviate nanoparticle aggregation and facilitate the separation and recovery of catalysts, but also exhibit enhanced visible-light photocatalytic performances (e.g., in photocatalytic coupling of amines to imines [22] and degradation of rhodamine B, phenol or tetracycline [21,23,24]) due to synergistic effects of enhanced visible-light utilization via multiple reflections and scattering, efficient separation of photo-generated electrons and holes and large surface area. In previous reports, hierarchical  $\text{BiOBr}$  microspheres of  $1.0\text{--}6.0\ \mu\text{m}$  in diameter were prepared in a two-component solvent (ethylene glycol and isopropanol [21] or water and ethanol [22]) with the assistance of a soft template (e.g., cetyltrimethylammo-

niium bromide [21,23], reactive ionic liquids [24] and poly(vinylpyrrolidone) (PVP) [22]) for the formation of self-assembled microspheres.

Herein hierarchical BiOBr microspheres of  $2.57 \pm 0.49 \mu\text{m}$  (designated BiOBr-MS) were directly self-assembled without the assistance of a template via a facile solvothermal synthesis in triethylene glycol (TEG) at  $150 \text{ }^\circ\text{C}$  for 3 h. The addition of PVP during solvothermal synthesis of BiOBr-MS significantly reduces the particle size to generate BiOBr sub-microspheres of  $0.87 \pm 0.25 \mu\text{m}$  (designated BiOBr-sMS). Both BiOBr-MS and BiOBr-sMS were evaluated as photocatalysts for aerobic photooxidation of BzOH under simulated sunlight irradiation. BiOBr-sMS had significantly improved photocatalytic performances (BzOH conversion and BzH selectivity and yield were 76.4%, 85.4% and 65.2%, respectively, upon Xenon irradiation for 3 h at  $25 \text{ }^\circ\text{C}$ ), which was attributed to its efficient charge separation, more negative conduction-band position and generation of larger amounts of  $\cdot\text{O}_2^-$  species. The  $\text{h}^+$  and  $\cdot\text{O}_2^-$  species were found to be main reactive species for the BzOH oxidation over BiOBr spheres by scavenging tests and spin-trapping EPR spectra. The present work demonstrated that the photocatalytic performance of the BiOBr semiconductor could be effectively enhanced by morphology modulation. It was achieved by using  $\text{KBrO}_3$  as a bromine source rather than organic templates, which slowly provides bromide ions during solvothermal treatment in TEG.

## 2. Results

### 2.1. Characterization of BiOBr-(s)MS

The XRD patterns of BiOBr-sMS and BiOBr-MS (Figure 1) are consistent with the standard pattern of tetragonal BiOBr (PDF No. 78-0348) without any impurity peak, indicating that pure BiOBr particles with good crystallinity were obtained whether PVP was added to the initial reaction mixture or not. In comparison with the standard XRD pattern, the relative intensity of the (110) diffraction peak was obviously enhanced, as observed in the literature [21,23]. This may be related to the hierarchical spherical morphology of BiOBr-(s)MS formed by self-assembly of nanoplates building units (SEM images shown below). During the XRD measurement, most nanoplates in hierarchical spheres would stand upright rather than lie flat on the XRD holder, which facilitates the exposure of more (110) facets to the incident X-ray beam and leads to the intensified (110) diffraction peak.

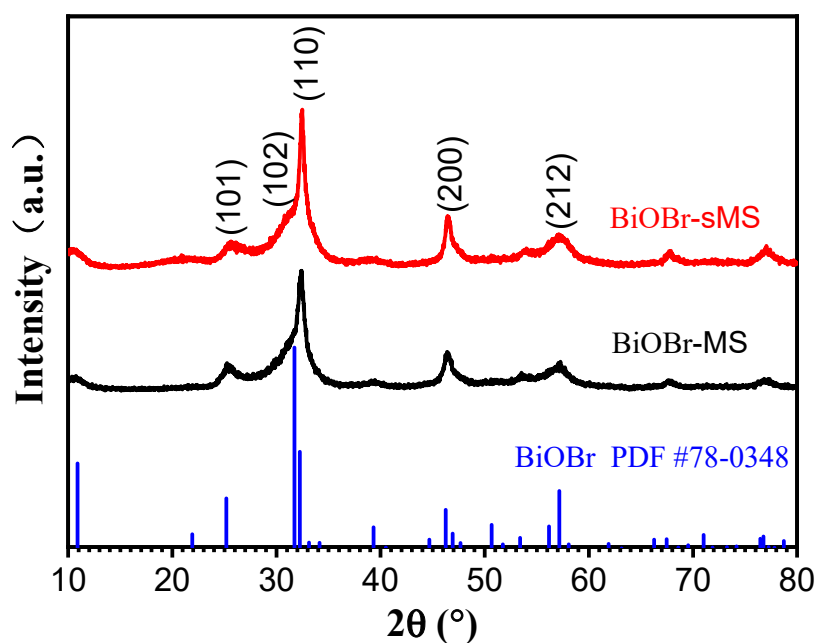
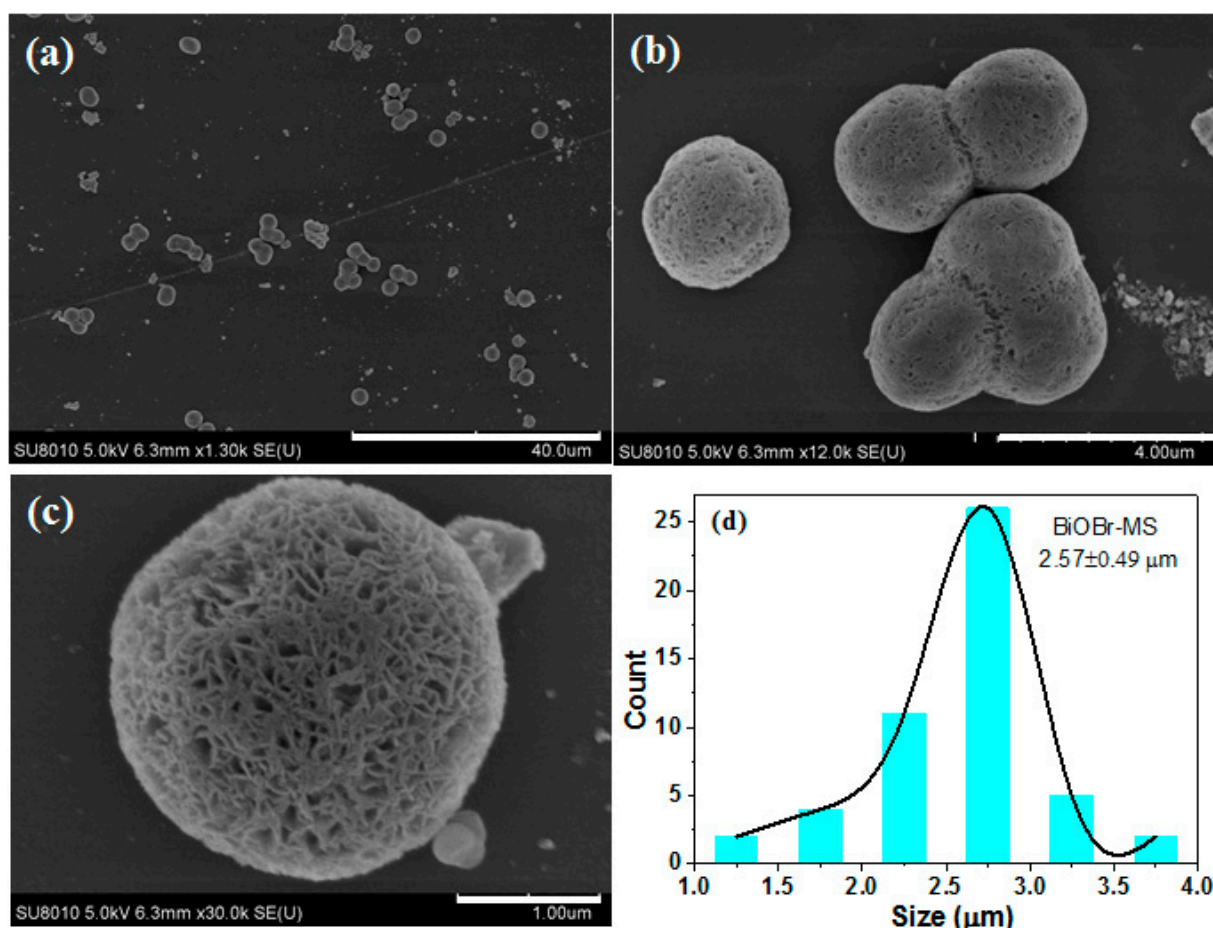


Figure 1. XRD patterns of BiOBr-sMS and BiOBr-MS.

In SEM images (Figure 2), BiOBr-MS particles are mostly microspheres of  $2.57 \pm 0.49 \mu\text{m}$  in diameter. Each microsphere possesses porous flower-like hierarchical structure formed by self-assembly of nanoplates of  $30.2 \pm 3.5 \text{ nm}$  in thickness (Figure 2c). It is worthy to note that the BiOBr-MS microspheres are directly self-assembled without the assistance of a template. In our method, TEG is a reducing solvent with a high-boiling point ( $\sim 285 \text{ }^\circ\text{C}$ ) [25–28]. During solvothermal treatment in TEG at  $150 \text{ }^\circ\text{C}$ ,  $\text{KBrO}_3$  will be gradually reduced to provide bromide ions for controlled growth and self-assembly of BiOBr-MS microspheres.



**Figure 2.** SEM images (a–c) and particle size histogram (d) of BiOBr-MS.

The addition of PVP during solvothermal synthesis of BiOBr-MS reduces the particle size by about three-fold to generate BiOBr-sMS sub-microspheres of  $0.87 \pm 0.25 \mu\text{m}$  in diameter, as revealed by its SEM and TEM images (Figure 3). In addition, the constituent nanoplates ( $24.8 \pm 2.8 \text{ nm}$  thick) in BiOBr-sMS microspheres are also thinner than those in BiOBr-MS. PVP has been generally exploited to make thin BiOX ( $X = \text{Cl}, \text{Br}$  or  $\text{I}$ ) nanosheets irrespective of different halogen ions [13,29,30]. Therefore, PVP mainly interacts with  $\text{Bi}^{3+}$  ions in the  $[\text{Bi}_2\text{O}_2]^{2-}$  layers of BiOBr-sMS via its carbonyl or amine functional groups of PVP molecules, and restricts the growth along the [001] direction to generate thinner BiOX nanoplates. Meanwhile, the polyvinyl chains of PVP adsorbed on the BiOBr-sMS nanoplates also contribute to their self-assembly process via van der Waals forces [22], inducing the formation of BiOBr-sMS with smaller particle sizes.

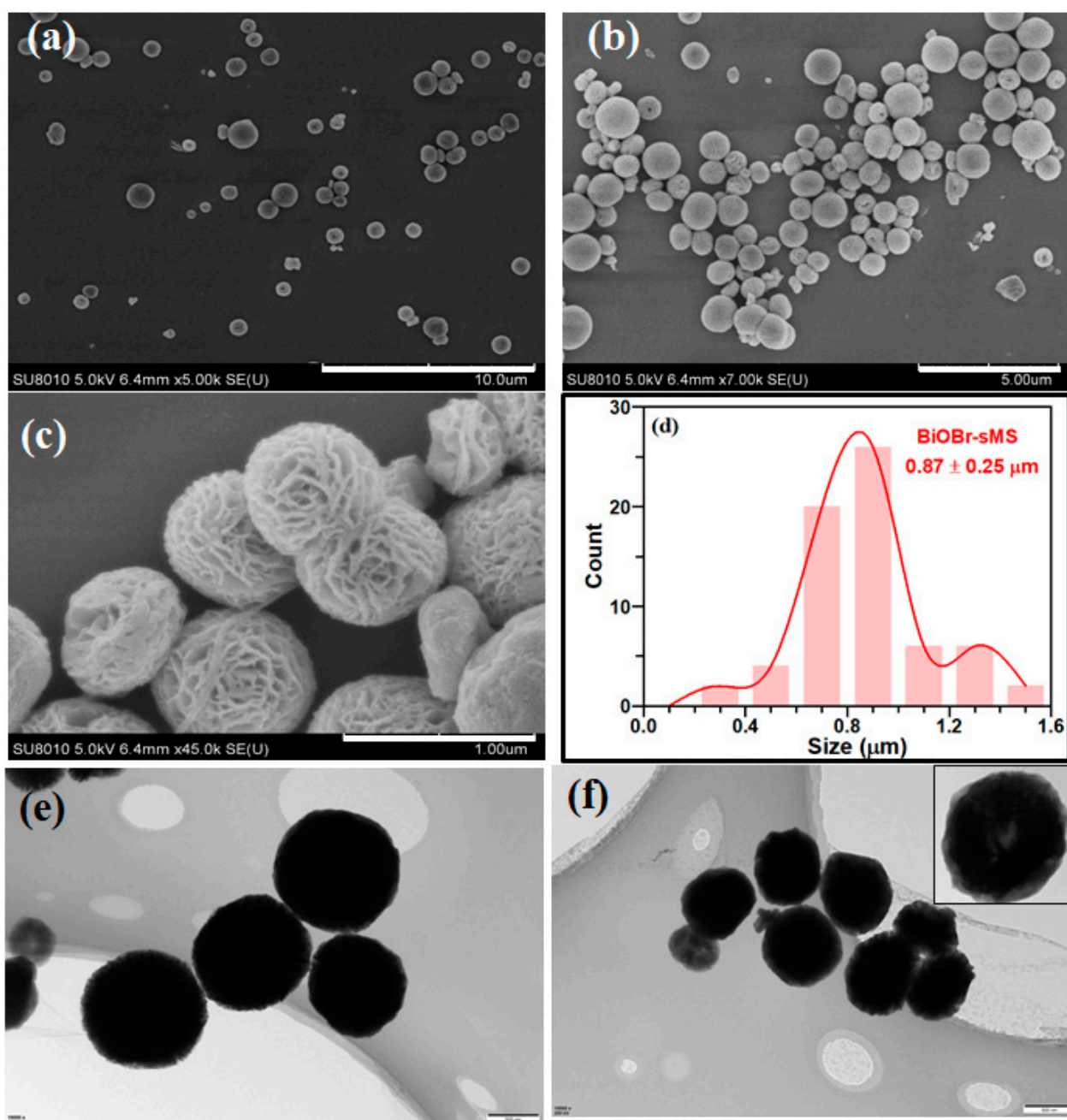


**Figure 3.** SEM (a–c), particle size histogram (d) and TEM images (e,f) of BiOBr-sMS.

The porous structures of BiOBr(s)MS were also supported by  $N_2$  adsorption–desorption isotherms (Figure 4). Both BiOBr-sMS and BiOBr-MS showed Type IV isotherm with H4 hysteresis loop between  $P/P_0 = 0.4$  and 1.0 according to IUPAC recommendation [31]. Type IV isotherms are typical of mesoporous adsorbents. The Type H4 loop is often associated with narrow slit-like pore. The  $S_{BET}$  and  $V_p$  values are  $18.8 \text{ m}^2/\text{g}$  and  $0.068 \text{ cm}^3/\text{g}$  for BiOBr-sMS, and  $36.9 \text{ m}^2/\text{g}$  and  $0.118 \text{ cm}^3/\text{g}$  for BiOBr-MS. The larger  $S_{BET}$  of BiOBr-MS is ascribed to its rich micropore, as manifested by higher adsorption at lower relative pressure in its  $N_2$  adsorption isotherm (Figure 4). The average pore diameter  $d_p$  (nm) was estimated by  $d_p = 4000V_p/S_{BET}$  [32–35] to be 14.5 nm for BiOBr-sMS and 12.8 nm for BiOBr-MS, which indicates that BiOBr-sMS has a more open hierarchical structure than BiOBr-MS.

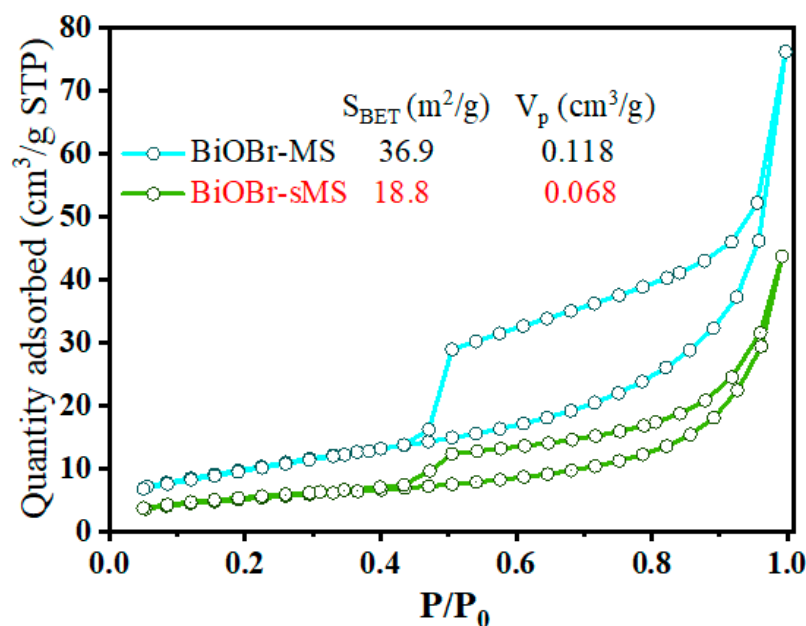


Figure 4.  $\text{N}_2$  adsorption–desorption isotherms of BiOBr-SMS and BiOBr-MS.

## 2.2. Photocatalytic Performances of BiOBr-(s)MS

The photocatalytic performances of BiOBr-sMS and BiOBr-MS were evaluated by simulated sunlight-driven aerobic photooxidation of BzOH to BzH (Figure 5). After illumination with Xenon lamp for 2 h, the BzOH conversions ( $C_{\text{BzOH}}$ ) over BiOBr-sMS and BiOBr-MS are 51.3% and 29.6%, respectively, with nearly 100% selectivity to BzH ( $S_{\text{BzH}}$ ). The high selectivity of BzH may be related to selective adsorption of BzOH via  $-\text{CH}_2\text{OH}$  group on BiOBr, which is beneficial for its selective oxidation by photo-generated surface reactive species (e.g., photo-holes and  $\cdot\text{O}_2^-$ ). However, as the photooxidation of BzOH on BiOBr-sMS proceeded,  $S_{\text{BzH}}$  gradually decreased (e.g., 67.0% at 4 h in Figure 6) due to further oxidation of BzH to benzoic acid. The photocatalytic activity of BiOBr-sMS is significantly higher than that of BiOBr-MS under Xenon lamp illumination. Since both BiOBr-sMS and BiOBr-MS were synthesized via the same synthetic procedure, except for the addition of PVP during the solvothermal synthesis of BiOBr-sMS, BiOBr-MS was post-treated with PVP as follows: 0.30 g of BiOBr-MS was stirred in 30 mL of DI water containing 0.40 g of PVP at room temperature for 1 h, centrifuged and then dried in a 60 °C vacuum oven overnight. The photocatalytic activity of the resulting control sample (denoted PVP/BiOBr-MS) was evaluated to clarify the role of PVP on the enhanced photocatalytic performance of BiOBr-sMS. As shown in Figure 5, PVP/BiOBr-MS has the lowest activity among the three samples (2 h BzOH conversion in the order of 11.6%, 29.6% and 51.3%). It indicated that the post-modification of BiOBr-MS by PVP deteriorated the photocatalytic activity of BiOBr-MS, possibly by blocking some active surface sites. Since physically adsorbed PVP could not improve the activity of BiOBr-sMS, it implied the importance of PVP in modulating the growth and self-assembly of BiOBr-sMS during its synthesis, which resulted in smaller, three-dimensional, hierarchical porous sub-microspheres made up of thinner nanoplates.

The photooxidation products of BzOH over BiOBr-sMS at different illumination times were analyzed to obtain more information about its kinetic process. As shown in Figure 6,  $C_{\text{BzOH}}$  increased with the illumination time. Upon illumination by Xe lamp for 4 h, 96.5% of 50 mM BzOH was converted, which is among the highest conversion achieved on single-component BiOBr photocatalysts for visible light-driven photooxidation of BzOH with a high-initial concentration (50 mM) (Table 1). However,  $S_{\text{BzH}}$  gradually decreased with illumination ( $S_{\text{BzH}}$ : 100% at 2 h and 67.0% at 4 h). The decrease in  $S_{\text{BzH}}$  after illumination for 4 h may be due to the high concentration of BzH accumulated in the reaction system, which was further oxidized to benzoic acid. As a result, the yield of BzH ( $Y_{\text{BzH}}$ ) was almost

constant after illumination for 3 h (64.7–65.2%). It is interesting to note that the  $C_{\text{BzOH}}$ -time plot in Figure 6 was excellently fitted with a linear equation,  $C_{\text{BzOH}} = 0.249t$  ( $R^2 = 0.999$ ). It indicated that the photocatalytic oxidation of BzOH over BiOBr-sMS conformed to the zero-order reaction model with the rate constant of  $k_0 = 12.5 \text{ mmol L}^{-1} \text{ h}^{-1}$ . Similarly, the  $C_{\text{BzOH}}$ -time plots over BiOBr-MS and PVP/BiOBr-MS could also be fitted into the zero-order reaction model with the corresponding  $k_0$  value of 6.7 and  $3.0 \text{ mmol L}^{-1} \text{ h}^{-1}$  (Figure S1). The largest  $k_0$  value of BiOBr-sMS is consistent with its highest activity.

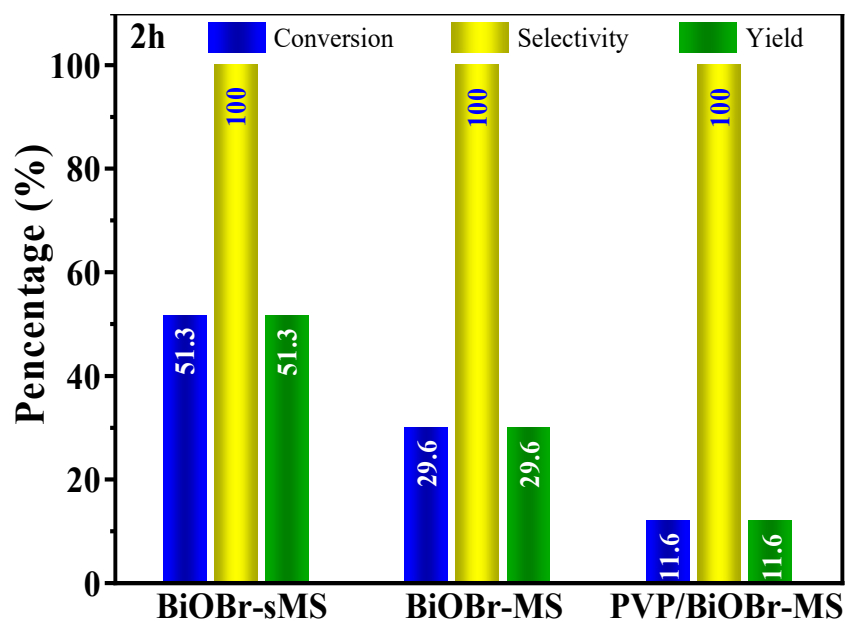


Figure 5. Photocatalytic performances of BiOBr-(s)MS. Reaction conditions: 20 mg catalyst,  $\text{O}_2$  balloon and 50 mM BzOH in 10 mL  $\text{CH}_3\text{CN}$ , illuminated with Xenon lamp for 2 h.

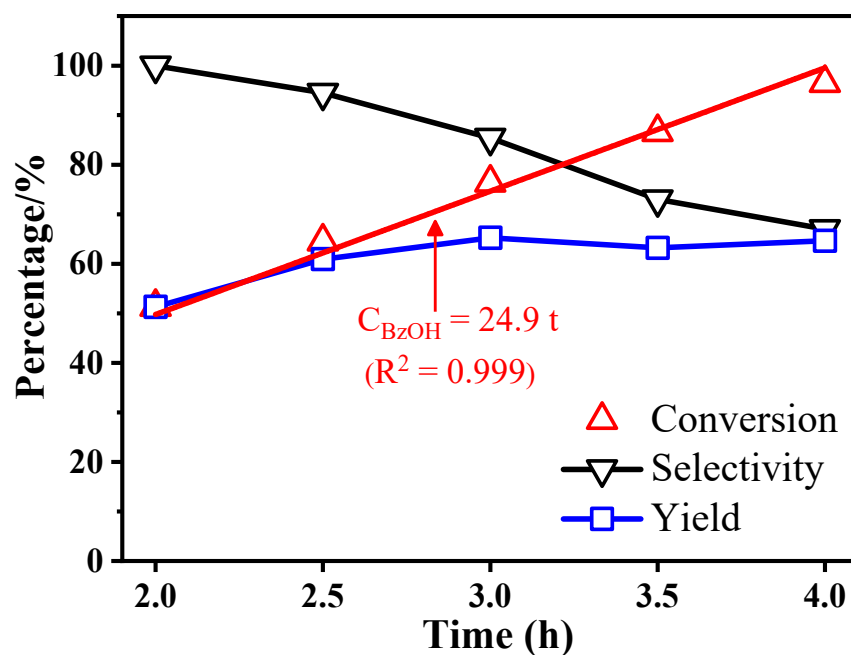


Figure 6. Time-dependent photocatalytic aerobic oxidation of BzOH over BiOBr-sMS. Reaction conditions: 20 mg BiOBr-sMS,  $\text{O}_2$  balloon and 50 mM BzOH in 10 mL  $\text{CH}_3\text{CN}$ , illuminated with Xenon lamp.

**Table 1.** Comparison of catalytic performances of various photocatalysts under Xe lamp illumination.

Entry	Photocatalyst	Conditions	Convsn/Sel/Yield (%)	Ref.
1	BiOBr-sMS	20 mg catalyst, 0.5 mmol BzOH, O <sub>2</sub> balloon, 10 mL CH <sub>3</sub> CN, 25 °C, 2 h	51.3%/100%/51.3% (96.5%/67.0%/64.7% at 4 h)	This work
2	WO <sub>2.72</sub>	0.1 g catalyst, 25 mmol BzOH, O <sub>2</sub> (20 mL/min), 60 mL BTF, 25 °C, 8 h	9.5%/91.0%/8.6%	[5]
3	WO <sub>2.72</sub> /rGO	0.1 g catalyst, 25 mmol BzOH, O <sub>2</sub> (20 mL/min), 60 mL BTF, 25 °C, 8 h	37.6%/92.0%/34.6%	[5]
4	Fluorinated mesoporous WO <sub>3</sub>	0.1 g catalyst, 0.025 mmol BzOH, 50 mL H <sub>2</sub> O, 25 °C, 4 h.	~57%/~99%/56%	[8]
5	Hybrid-SiW <sub>11</sub> O <sub>39</sub>	40 mg catalyst, 1 mmol BzOH, 3 mL CH <sub>3</sub> CN purged with O <sub>2</sub> , 25 °C, 4 h	80% yield	[7]
6	0.8Br-BiOBr /Bi <sub>2</sub> WO <sub>6</sub>	20 mg catalyst, 0.2 mmol BzOH, 2.5 mL BTF saturated with O <sub>2</sub> , 25 °C, 4 h	30.9%/100%/30.9%	[14]
7	TiO <sub>2</sub>	0.3 g catalyst, 25 mmol BzOH, 27 mL BTF, air bubbled at 20 mL/min, 5 h, (temperature unavailable)	21.6%/91.4%/19.7%	[36]
8	Nb <sub>2</sub> O <sub>5</sub> /TiO <sub>2</sub>	0.3 g catalyst, 25 mmol BzOH, 27 mL BTF, air bubbled at 20 mL/min, 5 h, (temperature unavailable)	64.3%/85.1%/54.7%	[36]
9	Ni(1%)-OTiO <sub>2</sub>	80 mg catalyst, 0.5 mmol BzOH, 5 mL BTF saturated with O <sub>2</sub> (2atm) for 5 min, 1 h (temperature unavailable)	93%/99%/88%	[9]

### 2.3. Mechanistic Studies of Enhanced Photocatalytic Activity of BiOBr-sMS

It is generally accepted that the photocatalytic activity is affected by various factors, such as specific surface area, band-gap energy, band position and separation efficiency of photo-induced electrons and holes. The BET surface areas of BiOBr-sMS and BiOBr-MS are 18.8 and 36.9 m<sup>2</sup>/g, respectively. Therefore, the surface area may not be the key factor contributing to the enhanced photocatalytic activity of BiOBr-sMS. However, BiOBr-sMS has larger average pore diameter than BiOBr-MS (14.5 vs. 12.8 nm), which should benefit the mass transport and diffusion in BiOBr-sMS.

UV-vis absorption spectra of BiOBr-(s)MS are shown in Figure 7a. As compared to BiOBr-MS, the absorption onset of BiOBr-sMS shifted to a shorter wavelength by about 17 nm (398 vs. 415 nm) with lower absorbance. Thus BiOBr-sMS utilizes less visible and ultra-violet light of the total solar energy, which cannot explain its improved photocatalytic activity either. The band-gap energy, E<sub>g</sub>, was estimated by Tauc plots according to  $\alpha h\nu = A(h\nu - E_g)^{n/2}$ , where  $\alpha$ ,  $\nu$  and A are the absorption coefficient, light frequency and a constant, respectively, and n is a constant that depends on the characteristics of the optical transition in a semiconductor (n = 1 for a direct transition and n = 4 for an indirect transition). For BiOBr, as an indirect gap semiconductor, the value of n is 4 [13,19,37]. By extrapolating the  $\alpha h\nu - (h\nu)^{1/2}$  plots to the x axis (Figure 8 inset), the E<sub>g</sub> values of BiOBr-MS and BiOBr-sMS are estimated to be 2.75 eV and 2.85 eV, respectively. The larger band-gap energy of BiOBr-sMS is ascribed to its smaller particle size.

Theoretical calculation reveals that the conduction and valance bands of BiOBr consist of Bi 6p, O 2p and Br 4p orbital [37,38]. The O 2p and Br 4p states dominate the valance-band (VB) maximum, while Bi 6p states contribute the most to the conduction-band (CB) minimum [38]. Both BiOBr-MS and BiOBr-sMS have similar compositions except the involvement of PVP during the solvothermal synthesis of BiOBr-sMS. Since PVP mainly interacts with the Bi<sup>3+</sup> ions via its carbonyl or amine functional groups, it is reasonable to assume that PVP mainly influences the CB position of BiOBr-sMS while both BiOBr-MS and BiOBr-sMS have similar VB positions. As the band-gap energy of BiOBr-sMS is larger than that of BiOBr-MS by 0.10 eV, the CB minimum of BiOBr-sMS is expected to shift upwards by 0.10 eV. As compared to BiOBr-MS, the more negative CB position of BiOBr-sMS is expected to facilitate the reduction of adsorbed molecular oxygen to generate more

superoxide radical anions ( $\cdot\text{O}_2^-$ ), which was collaborated by the following scavenging tests and spin-trapped EPR spectra. The generation of more  $\cdot\text{O}_2^-$  contributes to the enhanced photocatalytic activity of BiOBr-sMS.

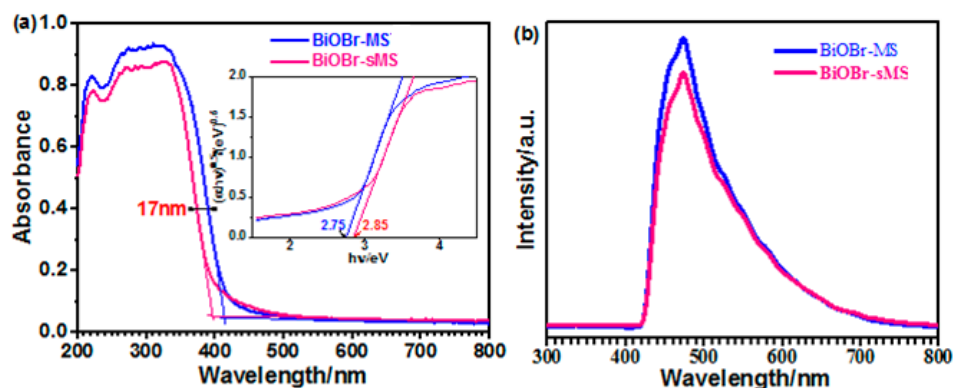


Figure 7. UV-vis spectra (a) and photoluminescence spectra (b) of BiOBr-sMS. Inset of (a) is the corresponding Tauc plots of  $(\alpha h\nu)^{1/2}-(h\nu)$ .

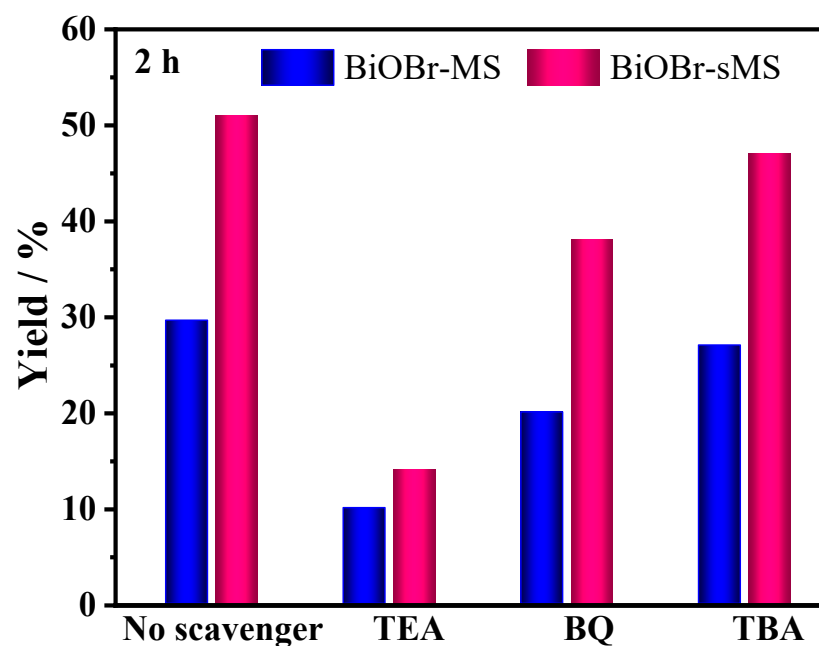


Figure 8. Trapping experiments of photocatalytic oxidation of BzOH over BiOBr-(s)MS.

Photoluminescence (PL) spectroscopy is generally used to evaluate the recombination rate of photo-excited charge carriers. The stronger PL intensity suggests rapid recombination of photoelectrons and holes. As displayed in Figure 7b, the PL spectrum of BiOBr-sMS had lower intensity than that of BiOBr-MS due to the reduced charge recombination in the former. It implied more efficient separation of photo-induced electrons and holes in BiOBr-sMS, which also contributes to its enhanced photocatalytic performance.

A series of active species trapping experiments were conducted to further investigate the photooxidation mechanism of BzOH. When triethanolamine (TEA) was added to the BzOH system to trap the holes ( $h^+$ ) [3], the BzOH conversion decreased significantly (e.g., from 51.0% to 14.2% over BiOBr-sMS in Figure 8), revealing that the photo-generated holes are the major oxidative species for the selective oxidation of BzOH into BzH. The addition of p-benzoquinone to trap superoxide radical anions ( $\cdot\text{O}_2^-$ ) also decreased the conversion of BzOH but to a lesser extent (e.g., from 51.0% to 38.0% over BiOBr-sMS in Figure 8), supporting partial contribution of  $\cdot\text{O}_2^-$  to the oxidation of BzOH. However,

when tert-butanol was added to trap hydroxyl radicals [39,40], no obvious influence on the BzOH conversion was observed (e.g., from 51.0% to 47.2% over BiOBr-sMS in Figure 8), suggesting a negligible contribution of hydroxyl radicals to the oxidation of BzOH in our photocatalytic reaction systems. The same reactive species ( $h^+$  and  $\cdot O_2^-$ ) responsible for the oxidation of BzOH to BzH were also found in other photocatalytic systems (e.g., Ni-OTiO<sub>2</sub> [9]).

EPR spectra were collected with DMPO a spin-trapping agent to identify the generation of  $\cdot O_2^-$ . Strong characteristic signals of DMPO- $\cdot O_2^-$  adduct were observed over BiOBr-sMS and BiOBr-MS under Xenon illumination [3,19], confirming the formation of superoxide radicals (Figure 9). In contrast, no EPR signal was detected in darkness (Figure 9). As compared with BiOBr-MS, the signal intensities of DMPO- $\cdot O_2^-$  adduct generated over BiOBr-sMS were stronger (the difference curve between BiOBr-sMS and BiOBr-MS displayed in Figure 9), indicating the formation of more  $\cdot O_2^-$  over BiOBr-sMS, due to its more negative CB position, which also contributed to its enhanced photocatalytic activity.

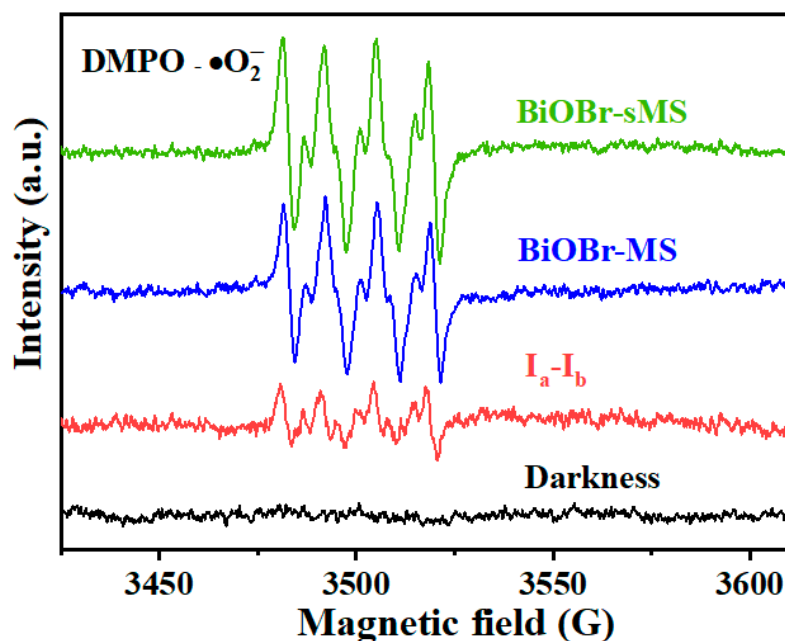


Figure 9. DMPO- $O_2^-$  spin-trapping EPR spectra of BiOBr-(s)MS.

### 3. Materials and Methods

#### 3.1. Chemicals Reagents

Bismuth nitrate pentahydrate ( $Bi(NO_3)_3 \cdot 5H_2O$ ) and benzaldehyde (BzH) were purchased from Aladdin (Shanghai, China).  $KBrO_3$ , triethylene glycol (TEG), acetonitrile ( $CH_3CN$ ), benzyl alcohol (BzOH), octane ( $C_8H_{18}$ ), triethanolamine (TEA) and p-quinone (BQ) were provided by Sinopharm Chemical Reagent, China. Tert-butanol (TBA) was obtained from Shanghai Macklin Biochemical, China. Poly(vinylpyrrolidone) (PVP, Mw: 55,000) and 5,5-dimethyl-1-pyrrolidine N-oxide (DMPO) were supplied by Sigma-Aldrich (Shanghai, China). All chemicals were of analytical reagents and used as received. All solutions were prepared in deionized (DI) water.

#### 3.2. Solvothermal Synthesis of BiOBr-(s)MS

BiOBr-sMS was made as follows: 0.4851 g (1.0 mmol) of  $Bi(NO_3)_3 \cdot 5H_2O$  was first dissolved in 25 mL of TEG upon sonication and magnetic stirring. Then, 0.4 g of PVP was added and stirred for 30 min, followed by the addition of 0.1670 g (1.0 mmol) of  $KBrO_3$ . After being stirred for another 1 h, the whole reaction mixture was transferred to a

50-mL autoclave and heated at 150 °C for 3 h. The BiOBr-sMS particles were recovered by centrifugation, washed five times with DI water and dried in a 60 °C vacuum for 12 h.

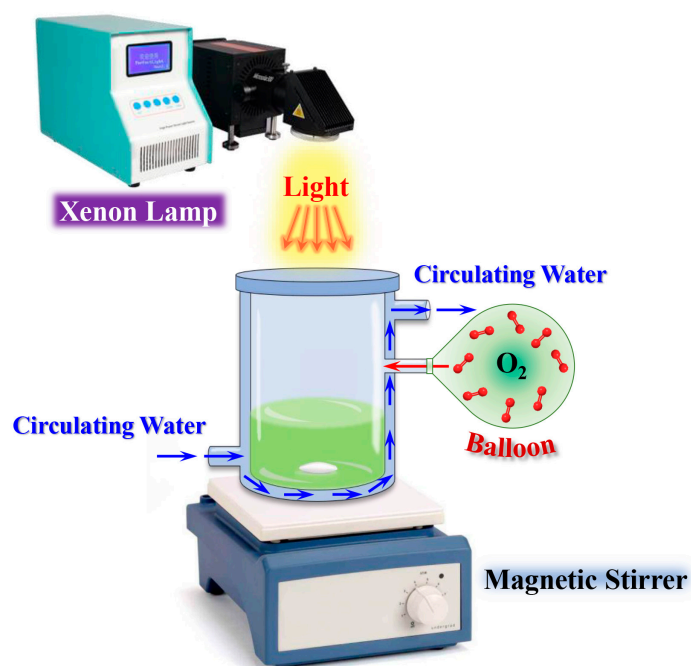
BiOBr-MS was prepared following the same procedure except that no PVP was added in initial reaction mixture.

### 3.3. Characterization

The crystal structure was determined by powder X-ray diffractometer (XRD, Bruker AXS D8 Advance, Karlsruhe, Germany) with Cu K $\alpha$  (1.5406 Å) as the X-ray source in the 2 $\theta$  range of 10°~80° at a scanning speed of 5°/min. The morphology was observed by a scanning electron microscope (SEM, Hitachi SU8010, Tokyo, Japan). UV-vis diffuse reflectance spectra (DRS, Tpkyo, Japan) were collected on the Hitachi UH4150 UV-vis spectrometer with BaSO<sub>4</sub> as a reference, and converted from reflection to absorbance by the Kubelka-Munk method. Photoluminescence (PL) spectra were performed via the Hitachi F-4600 fluorescence spectrophotometer with an excitation wavelength at 320 nm. N<sub>2</sub> adsorption–desorption isotherms were measured on Micromeritics ASAP 2020 analyzer (USA). All samples were degassed at 150 °C for 4 h under vacuum before measurement. The specific surface area was calculated using the BET method ( $S_{\text{BET}}$ ) from adsorption data in a relative pressure range from 0.05 to 0.30. The pore volume ( $V_p$ ) was assessed from the adsorbed amount at a relative pressure of 0.99.

### 3.4. Photocatalytic Aerobic Oxidation of BzOH over BiOBr Nanostructures

In a typical process, 20 mg of BiOBr-sMS was first stirred in 10 mL of BzOH (50 mM) solution in CH<sub>3</sub>CN in a closed double-wall quartz cell in the dark at room temperature for 30 min to reach the adsorption equilibrium. The reaction temperature was controlled by circulating water. The quartz cell was connected to a balloon full of molecular oxygen (Scheme 2). Then, the suspension was illuminated from the top for 2–4 h with a 225 W Xe lamp (CEL-PF300-T8, Beijing China Education AuLight Technology, Beijing, China) to simulate sunlight. At certain intervals, about 1.5 mL of suspension was sampled, centrifuged and filtered through a filter membrane. The product was analyzed with n-octane as an internal standard on the Fuli 9720 gas chromatograph (China) fitted with a FID detector. The catalytic experiments were repeated with the standard deviation of about 5%.



**Scheme 2.** Illustration of the photoreaction system used in this work.

### 3.5. Scavenging and Spin-Trapping Tests

TEA (66  $\mu\text{L}$ ), BQ (0.0541 g) and TBA (48  $\mu\text{L}$ ) were added to scavenge  $\text{h}^+$ ,  $\cdot\text{O}_2^-$  and  $\cdot\text{OH}$ , respectively, during photocatalytic aerobic oxidation of BzOH, as described in Section 3.4. In spin-trapping studies, DMPO was used as a trapping agent to detect  $\cdot\text{O}_2^-$  by electron paramagnetic resonance (EPR) spectra, which were recorded on the Bruker EMXplus Spectrometer at room temperature.

## 4. Conclusions

Porous hierarchical BiOBr microspheres (BiOBr-MS) of  $2.57 \pm 0.49 \mu\text{m}$  were first self-assembled without the assistance of a template via a facile solvothermal synthesis in triethylene glycol (TEG) at  $150^\circ\text{C}$  for 3 h. The slow release of bromide ions upon reduction of  $\text{KBrO}_3$  in TEG facilitated the controlled growth and self-assembly of primary BiOBr nanoplates. The addition of PVP during solvothermal synthesis of BiOBr-MS reduced the particle size by nearly three-fold to generate BiOBr sub-microspheres (BiOBr-sMS) of  $0.87 \pm 0.25 \mu\text{m}$ . BiOBr-sMS exhibited remarkably improved photocatalytic activity than BiOBr-MS for aerobic photooxidation of benzyl alcohol (BzOH) to benzaldehyde (BzH) under simulated sunlight irradiation (the conversions of BzOH (50 mM) over BiOBr-sMS and BiOBr-MS were, respectively, 51.3% and 29.6% with 100% selectivity to BzH after Xenon illumination for 2 h at  $25^\circ\text{C}$ ). Scavenging tests and DMPO- $\text{O}_2^-$  spin-trapping EPR spectra supported that photogenerated holes ( $\text{h}^+$ ) and  $\cdot\text{O}_2^-$  were the main reactive species for the BzOH oxidation over BiOBr spheres. The higher photocatalytic activity of BiOBr-sMS was attributed to its more open hierarchical structure, efficient charge separation, more negative conduction-band position and the generation of larger amounts of  $\cdot\text{O}_2^-$  species.

**Supplementary Materials:** The following supporting information can be downloaded at: <https://www.mdpi.com/article/10.3390/catal13060958/s1>, Figure S1: Time-dependent aerobic photo-oxidation of BzOH over BiOBr nanostructures.

**Author Contributions:** Z.W.: Resource, Formal analysis, Writing—Original Draft. C.L.: Investigation, Methodology, Validation. F.C.: Conceptualization, Writing—Review and Editing. R.C.: Funding acquisition, Writing—Review and Editing. All authors have read and agreed to the published version of the manuscript.

**Funding:** This work was supported by the National Natural Science Foundation of China (22076149) and Special Project of State Key Laboratory of New Textile Materials & Advanced Processing Technologies from Wuhan Science and Technology Bureau (2022013988065204).

**Data Availability Statement:** Data are available within the article.

**Conflicts of Interest:** The authors declare no conflict of interest.

## References

1. Brühne, F.; Wright, E. *Benzaldehyde*; Wiley-VCH Verlag GmbH & Co. KGaA: Hoboken, NJ, USA, 2000.
2. Rak, M.J.; Lerro, M.; Moores, A. Hollow iron oxide nanoshells are active and selective catalysts for the partial oxidation of styrene with molecular oxygen. *Chem. Commun.* **2014**, *50*, 12482–12485. [[CrossRef](#)] [[PubMed](#)]
3. Xiao, X.; Jiang, J.; Zhang, L. Selective oxidation of benzyl alcohol into benzaldehyde over semiconductors under visible light: The case of  $\text{Bi}_{12}\text{O}_{17}\text{Cl}_2$  nanobelts. *Appl. Catal. B Environ.* **2013**, *142–143*, 487–493. [[CrossRef](#)]
4. Schultz, D.M.; Yoon, T.P. Solar synthesis: Prospects in visible light photocatalysis. *Science* **2014**, *343*, 1239176. [[CrossRef](#)] [[PubMed](#)]
5. Ma, B.; Huang, E.; Wu, G.; Dai, W.; Guan, N.; Li, L. Fabrication of  $\text{WO}_{2.72}/\text{RGO}$  nano-composites for enhanced photocatalysis. *RSC Adv.* **2017**, *7*, 2606–2614. [[CrossRef](#)]
6. Li, P.; Zhao, H.; Yan, X.; Yang, X.; Li, J.; Gao, S.; Cao, R. Visible-light-driven photocatalytic hydrogen production coupled with selective oxidation of benzyl alcohol over  $\text{CdS@MoS}_2$  heterostructures. *Sci. China Mater.* **2020**, *63*, 2239–2250. [[CrossRef](#)]
7. Karimian, D.; Yadollahi, B.; Mirkhani, V. Harvesting visible light for aerobic oxidation of alcohols by a novel and efficient hybrid polyoxometalate. *Dalton Trans.* **2015**, *44*, 1709–1715. [[CrossRef](#)]
8. Su, Y.; Han, Z.; Zhang, L.; Wang, W.; Duan, M.; Li, X.; Zheng, Y.; Wang, Y.; Lei, X. Surface hydrogen bonds assisted meso-porous  $\text{WO}_3$  photocatalysts for high selective oxidation of benzylalcohol to benzylaldehyde. *Appl. Catal. B Environ.* **2017**, *217*, 108–114. [[CrossRef](#)]

9. She, H.; Zhou, H.; Li, L.; Wang, L.; Huang, J.; Wang, Q. Nickel-doped excess oxygen defect titanium dioxide for efficient selective photocatalytic oxidation of benzyl alcohol. *ACS Sustain. Chem. Eng.* **2018**, *6*, 11939–11948. [[CrossRef](#)]
10. Lam, S.-M.; Jaffari, Z.H.; Sin, J.-C.; Zeng, H.; Lin, H.; Li, H.; Mohamed, A.R. Insight into the influence of noble metal decorated on BiFeO<sub>3</sub> for 2,4-dichlorophenol and real herbicide wastewater treatment under visible light. *Colloids Surf. A Physicochem. Eng. Asp.* **2021**, *614*, 126138. [[CrossRef](#)]
11. Chin, Y.-H.; Sin, J.-C.; Lam, S.-M.; Zeng, H.; Lin, H.; Li, H.; Huang, L.; Mohamed, A.R. 3-D/3-D Z-scheme heterojunction composite formed by marimo-like Bi<sub>2</sub>WO<sub>6</sub> and mammillaria-like ZnO for expeditious sunlight photodegradation of dimethyl phthalate. *Catalysts* **2022**, *12*, 1427. [[CrossRef](#)]
12. Li, J.; Yu, Y.; Zhang, L. Bismuth oxyhalide nanomaterials: Layered structures meet photocatalysis. *Nanoscale* **2014**, *6*, 8473–8488. [[CrossRef](#)]
13. Chen, J.; Guan, M.; Cai, W.; Guo, J.; Xiao, C.; Zhang, G. The dominant {001} facet-dependent enhanced visible-light photoactivity of ultrathin BiOBr nanosheets. *Phys. Chem. Chem. Phys.* **2014**, *16*, 20909–20914. [[CrossRef](#)] [[PubMed](#)]
14. Wang, F.J.; Gu, Y.Y.; Yang, Z.Y.; Xie, Y.Y.; Zhang, J.J.; Shang, X.T.; Zhao, H.B.; Zhang, Z.Z.; Wang, X.X. The effect of halogen on BiOX (X = Cl, Br, I)/Bi<sub>2</sub>WO<sub>6</sub> heterojunction for visible-light-driven photocatalytic benzyl alcohol selective oxidation. *Appl. Catal. A-Gen.* **2018**, *567*, 65–72. [[CrossRef](#)]
15. Bisht, N.S.; Mehta, S.P.S.; Sahoo, N.G.; Dandapat, A. The room temperature synthesis of a CuO-Bi-BiOBr ternary Z-scheme photocatalyst for enhanced sunlight driven alcohol oxidation. *Dalton Trans.* **2021**, *50*, 5001–5010. [[CrossRef](#)]
16. Wang, X.; Zhang, Y.; Xu, H.; Ji, X.; Gan, L.; Zhang, R. Sugar-regulated bismuth oxybromide flowers with active imprinting sites for efficient photooxidative ability. *J. Alloys Compd.* **2021**, *879*, 160374. [[CrossRef](#)]
17. Bisht, N.S.; Pancholi, D.; Sahoo, N.G.; Melkani, A.B.; Mehta, S.P.S.; Dandapat, A. Effect of Ag-Fe-Cu tri-metal loading in bismuth oxybromide to develop a novel nanocomposite for the sunlight driven photocatalytic oxidation of alcohols. *Catal. Sci. Technol.* **2019**, *9*, 3923–3932. [[CrossRef](#)]
18. Sin, J.C.; Lam, S.M.; Zeng, H.; Lin, H.; Li, H.; Huang, L.; Liaw, S.J.; Mohamed, A.R.; Lim, J.W. Construction of visible light-driven Eu-doped BiOBr hierarchical microflowers for ameliorated photocatalytic 2,4-dichlorophenol and pathogens decomposition with synchronized hexavalent chromium reduction. *Mater. Today Sustain.* **2023**, *22*, 100340. [[CrossRef](#)]
19. Wang, H.; Yong, D.; Chen, S.; Jiang, S.; Zhang, X.; Shao, W.; Zhang, Q.; Yan, W.; Pan, B.; Xie, Y. Oxygen-vacancy-mediated exciton dissociation in BiOBr for boosting charge-carrier-involved molecular oxygen activation. *J. Am. Chem. Soc.* **2018**, *140*, 1760–1766. [[CrossRef](#)]
20. Dai, R.; Zhang, L.; Ning, J.; Wang, W.; Wu, Q.; Yang, J.; Zhang, F.; Wang, J.-A. New insights into tuning BiOBr photocatalysis efficiency under visible-light for degradation of broad-spectrum antibiotics: Synergistic calcination and doping. *J. Alloys Compd.* **2021**, *887*, 161481. [[CrossRef](#)]
21. Huo, Y.; Zhang, J.; Miao, M.; Jin, Y. Solvothermal synthesis of flower-like BiOBr microspheres with highly visible-light photocatalytic performances. *Appl. Catal. B Environ.* **2012**, *111–112*, 334–341. [[CrossRef](#)]
22. Juntrapirom, S.; Tantraviwat, D.; Anuchai, S.; Thongsook, O.; Channei, D.; Inceesungvorn, B. Boosting photocatalytic coupling of amines to imines over BiOBr: Synergistic effects derived from hollow microsphere morphology. *J. Environ. Chem. Eng.* **2021**, *9*, 106732. [[CrossRef](#)]
23. Ahmad, A.; Meng, X.C.; Yun, N.; Zhang, Z.S. Preparation of hierarchical BiOBr microspheres for visible light-induced photocatalytic detoxification and disinfection. *J. Nanomater.* **2016**, *2016*, 1373725. [[CrossRef](#)]
24. Nan, Q.; Huang, S.; Zhou, Y.; Zhao, S.; He, M.; Wang, Y.; Li, S.; Huang, T.; Pan, W. Ionic liquid-assisted synthesis of porous BiOBr microspheres with enhanced visible light photocatalytic performance. *Appl. Organomet. Chem.* **2018**, *32*, e4596. [[CrossRef](#)]
25. Grabs, I.-M.; Bradtmöller, C.; Menzel, D.; Garneting, G. Formation mechanisms of iron oxide nanoparticles in different nonaqueous media. *Cryst. Growth Des.* **2012**, *12*, 1469–1475. [[CrossRef](#)]
26. Cai, W.; Wan, J. Facile synthesis of superparamagnetic magnetite nanoparticles in liquid polyols. *J. Colloid Interface Sci.* **2007**, *305*, 366–370. [[CrossRef](#)] [[PubMed](#)]
27. Miguel-Sancho, N.; Bomati-Miguel, O.; Roca, A.G.; Martinez, G.; Arruebo, M.; Santamaria, J. Synthesis of magnetic nanocrystals by thermal decomposition in glycol media: Effect of process variables and mechanistic study. *Ind. Eng. Chem. Res.* **2012**, *51*, 8348–8357. [[CrossRef](#)]
28. Zhou, S.; Wang, C.; Xia, Y. Polyol synthesis of Pd icosahedral nanocrystals: Insights into the growth mechanism and size control. *Chem. Mater.* **2022**, *34*, 5065–5073. [[CrossRef](#)]
29. Guan, M.; Xiao, C.; Zhang, J.; Fan, S.; An, R.; Cheng, Q.; Xie, J.; Zhou, M.; Ye, B.; Xie, Y. Vacancy associates promoting solar-driven photocatalytic activity of ultrathin bismuth oxychloride nanosheets. *J. Am. Chem. Soc.* **2013**, *135*, 10411–10417. [[CrossRef](#)]
30. Di, J.; Xia, J.; Ji, M.; Xu, L.; Yin, S.; Chen, Z.; Li, H. Bidirectional acceleration of carrier separation spatially via N-CQDs/atomically-thin BiOI nanosheets nanojunctions for manipulating active species in a photocatalytic process. *J. Mater. Chem. A* **2016**, *4*, 5051–5061. [[CrossRef](#)]
31. Sing, K.S.W. Reporting physisorption data for gas/solid systems with special reference to the determination of surface area and porosity (Recommendations 1984). *Pure Appl. Chem.* **1985**, *57*, 603–619. [[CrossRef](#)]
32. Rabah, M.A.; Yasri, N.G.; Alaya, M.N. Impact of aging on the structural, textural, and acid properties of WO<sub>3</sub>-SO<sub>4</sub><sup>2-</sup>-SnO<sub>2</sub> solid acids. *J. Alloys Compd.* **2019**, *790*, 452–465. [[CrossRef](#)]

33. Ben, T.; Ren, H.; Ma, S.; Cao, D.; Lan, J.; Jing, X.; Wang, W.; Xu, J.; Deng, F.; Simmons, J.M.; et al. Targeted synthesis of a porous aromatic framework with high stability and exceptionally high surface area. *Angew. Chem. Int. Ed.* **2009**, *48*, 9457–9460. [[CrossRef](#)] [[PubMed](#)]
34. Ali, M.A.; Asaoka, S. Ni-Mo-titania-alumina catalysts with USY zeolite for low pressure hydrodesulfurization and hydrocracking. *Pet. Sci. Technol.* **2009**, *27*, 984–997. [[CrossRef](#)]
35. Al-Omair, M.A.; El-Sharkawy, E.A. Removal of heavy metals via adsorption on activated carbon synthesized from solid wastes. *Environ. Technol.* **2007**, *28*, 443–451. [[CrossRef](#)]
36. Yan, J.; Wu, G.; Guan, N.; Li, L. Nb<sub>2</sub>O<sub>5</sub>/TiO<sub>2</sub> heterojunctions: Synthesis strategy and photocatalytic activity. *Appl. Catal. B Environ.* **2014**, *152–153*, 280–288. [[CrossRef](#)]
37. Zhang, H.; Liu, L.; Zhou, Z. Towards better photocatalysts: First-principles studies of the alloying effects on the photocatalytic activities of bismuth oxyhalides under visible light. *Phys. Chem. Chem. Phys.* **2012**, *14*, 1286–1292. [[CrossRef](#)]
38. Xiao, X.; Liu, C.; Hu, R.; Zuo, X.; Nan, J.; Li, L.; Wang, L. Oxygen-rich bismuth oxyhalides: Generalized one-pot synthesis, band structures and visible-light photocatalytic properties. *J. Mater. Chem.* **2012**, *22*, 22840–22843. [[CrossRef](#)]
39. Chen, F.; Lv, H.; Chen, W.; Chen, R. Catalytic wet peroxide oxidation of anionic pollutants over fluorinated Fe<sub>3</sub>O<sub>4</sub> microspheres at circumneutral pH values. *Catalysts* **2022**, *12*, 1564. [[CrossRef](#)]
40. Guo, S.; Chen, M.; Huang, Y.; Wei, Y.; Ali, J.; Cai, C.; Wei, Q.S. Three-dimensionally printed zero-valent copper with hierarchically porous structures as an efficient Fenton-like catalyst for enhanced degradation of tetracycline. *Catalysts* **2023**, *13*, 446. [[CrossRef](#)]

**Disclaimer/Publisher’s Note:** The statements, opinions and data contained in all publications are solely those of the individual author(s) and contributor(s) and not of MDPI and/or the editor(s). MDPI and/or the editor(s) disclaim responsibility for any injury to people or property resulting from any ideas, methods, instructions or products referred to in the content.